

Mg_xZn_{1-x}O contact to CuGa₃Se₅ absorber for photovoltaic and photoelectrochemical devices

Imran S. Khan¹, Christopher P. Muzzillo¹, Craig L. Perkins¹, Andrew G. Norman¹, James Young¹,
Nicolas Gaillard², and Andriy Zakutayev¹

¹ National Renewable Energy Laboratory, Golden, CO, USA

² Hawaii Natural Energy Institute, University of Hawaii, Honolulu

Abstract:

CuGa₃Se₅ is a promising candidate material with wide band gap for top cells in tandem photovoltaic (PV) and photoelectrochemical (PEC) devices. However, traditional CdS contact layers used with other chalcopyrite absorbers are not suitable for CuGa₃Se₅ due to the higher position of its conduction band minimum. Mg_xZn_{1-x}O is a transparent oxide with adjustable band gap and conduction band position as a function of magnesium composition, but its direct application is hindered by CuGa₃Se₅ surface oxidation. Here, Mg_xZn_{1-x}O is investigated as a contact (n-type ‘buffer’ or ‘window’) material to CuGa₃Se₅ absorbers pretreated in Cd²⁺ solution, and an onset potential close to 1 V vs RHE in 10 mM hexaammineruthenium (III) chloride electrolyte is demonstrated. The Cd²⁺ surface treatment changes the chemical composition and electronic structure of the CuGa₃Se₅ surface, as demonstrated by photoelectron spectroscopy measurements. The performance of CuGa₃Se₅ absorber with Cd²⁺ treated surface in the solid-state test structure depends on the Zn/Mg ratio in the Mg_xZn_{1-x}O layer. The measured open circuit voltage close to 1 V is promising for tandem PEC water splitting with CuGa₃Se₅/Mg_xZn_{1-x}O top cells.

1. Introduction:

Hydrogen is considered one of the most promising means of storing renewable energy because it is the most abundant element in the world, has the highest energy density among non-nuclear fuels, and is a zero-emission fuel [1]. Solar photoelectrochemical (PEC) water splitting can be used to produce hydrogen, but a commercially viable PEC device technology remains elusive despite long research history [2]. Tandem monolithic PEC devices with a multijunction hybrid photoelectrode [3] consisting of group III-V semiconductors have been able to reach direct water splitting solar-to-hydrogen (STH) efficiency above 19% [4]. However, large scale commercial adoption of such technology is limited by high processing costs and finite durability during PEC water splitting. To maintain high efficiency and reduce processing cost, tandem PEC devices with chalcopyrite absorber materials can be adopted from photovoltaic (PV) research. These chalcopyrites have lower deposition cost and higher defect tolerance, which together with bandgap tunability makes them attractive for application in solar water splitting. Indeed, wide bandgap chalcopyrite CuGaSe_2 [5] [6], $\text{CuGa}(\text{S},\text{Se})_2$ [7] and $\text{Cu}(\text{In},\text{Ga})\text{S}_2$ [8] photocathodes have shown promising PEC performance and stability, and emerging wide bandgap CuGa_3Se_5 has been recently proposed [9].

CuGa_3Se_5 is an ordered-vacancy compound derived from the chalcopyrite structure of the well-known CuGaSe_2 absorber material by substituting Ga at Cu sites and leaving Cu sites vacant, $[2\text{V}_{\text{Cu}}^{-1} + \text{Ga}_{\text{Cu}}^{+2}]$ [10]. Reducing the Cu/Ga composition widens the band gap by reducing the valence band energy by ~ 0.2 eV, because of lower contribution from the Cu 3d states to the valence bands [11]. Due to its ideal bandgap of 1.84 eV and suitable conduction band alignment for H_2 evolution, CuGa_3Se_5 is a promising absorber material candidate for top cell applications in tandem PEC water splitting devices. Calculations show that if paired with a 1.23 eV bandgap

absorber in a tandem PEC cell, CuGa_3Se_5 could potentially lead to STH efficiency as high as 22.8% [12]. Initially a $\text{CuGa}_3\text{Se}_5/\text{ZnS}/\text{Pt}$ device with current output of $8 \text{ mA}/\text{cm}^2$ (0V vs RHE, 3-electrode) was reported [13], and subsequently the photocurrent density was increased up to $9.3 \text{ mA}/\text{cm}^2$ for a mixed phase of CuGaSe_2 and CuGa_3Se_5 with CdS-modified surface and Pt catalyst [14]. More recently, 17 days of continuous water splitting operation for a bare CuGa_3Se_5 absorber photocathode with $\sim 12 \text{ mA}/\text{cm}^2$ photocurrent at -1 V vs RHE have been demonstrated by our team, suggesting promising durability [9]. These encouraging outcomes clearly point out the need for further fundamental study of this absorber and its interface with other materials.

Traditional chalcopyrites CuGaSe_2 and ordered-vacancy CuGa_3Se_5 absorbers are often interfaced with CdS as a contact material (also known as n-type ‘buffer’ or ‘window’) to create the pn-junction. However, CdS contact layers suffer from short wavelength absorption and instability in electrolyte solution. In addition, CdS has a cliff-like $\sim 0.2 \text{ eV}$ conduction band (CB) offset with stoichiometric CuGaSe_2 , and a similar CB offset is expected for CuGa_3Se_5 [15]. If the conduction band minimum (CBM) of the contact is lower than that of the absorber (a ‘cliff’ type offset), the device suffers from lower photovoltage, increased interface recombination, and other detrimental effect to device performance [16] [17] [18]. If a CBM of the contact is more than 0.3 eV above that of the absorber (a ‘spike’ type offset), the resulting barrier impedes the collection of photo-generated carriers [19] [20] [21].

To address these challenges, $\text{Mg}_x\text{Zn}_{1-x}\text{O}$ (MZO) [22] [23] with tunable conduction band position as a function of Mg content has been proposed as an attractive n-type contact layer. MZO thin film was demonstrated with up to $x = 0.46$ grown by RF co-sputtering without any phase segregation resulting in a bandgap of up to 4.2 eV , while ZnO has a bandgap of 3.24 eV [22]. Combinatorial studies explored the composition spreads of MZO with different deposition

methods, such as pulsed laser deposition [24] [25] and chemical vapor deposition [26]. In a previous combinatorial study, we showed that the conduction band position could be tuned by 0.5 eV as Mg concentration changes from 4 to 12% [27], suggesting that it might be a suitable contact to CuGa₃Se₅ absorber. Integration of MZO as contact material resulted in significant efficiency improvements in different solar cell device technologies such as CdTe [28] and CIGS [29] [30], as well as CuGaSe₂ [31] that likely has similar CB position to CuGa₃Se₅.

In this study, MZO was investigated as the contact layer material for CuGa₃Se₅ absorber-based PV and PEC devices. Structural, optical and electrical properties of MZO thin films were studied as a function of different experimental conditions such as Mg composition, Ga doping, substrate temperature and deposition ambient. MZO depositions were performed by combinatorial radio frequency (RF) sputtering. For functional CuGa₃Se₅/MZO PV device, absorber surface pretreatment with Cd²⁺ solution was crucial because it removed surface oxidation, led to Cd incorporation, and possibly changed the surface conductivity type. MZO deposition and the surface pretreatment conditions were optimized for solid state solar cell performance. The outcome was a significant improvement in open circuit voltage (up to 920 mV) compared to conventional CdS-contact CuGa₃Se₅ devices (~730 mV). Replacement of CdS also improved quantum efficiency in the blue region of the spectrum. The PEC characteristics of CuGa₃Se₅/MZO as photocathode are tested with hexaammineruthenium (III) chloride sacrificial redox electrolyte, which exhibited an onset potential near 1 V vs reversible hydrogen electrode (RHE). These outcomes indicate that CuGa₃Se₅/Mg_xZn_{1-x}O could serve as an efficient top cell for tandem PV and PEC water splitting devices.

2. Experimental Methods:

2.1 Material synthesis and measurements

Ga-doped $\text{Mg}_x\text{Zn}_{1-x}\text{O}$ thin film sample libraries with orthogonal composition gradients of Mg and Ga were deposited by combinatorial RF magnetron sputtering from ZnO, Mg and Ga_2O_3 targets (Figure 1a). 50x50 mm Eagle XG glass substrates were cleaned with laboratory grade detergent followed by sonication in warm DI water, acetone and isopropanol. MZO depositions were done at a pressure of 3 mTorr in Ar/ O_2 atmosphere where the total gas flow rate was fixed at 16 sccm. The chamber base pressure was 5×10^{-7} Torr. O_2 flow, found to be crucial for good quality transparent films, was varied from 0.5 to 2% of the total gas flow for different depositions. A premixed 5% O_2 in Ar cylinder was used as O_2 source for precise flow control. A gas ring around the substrate carrying the O_2 lines ensured uniform O_2 containing environment across the substrate. The samples were mounted on a temperature calibrated Inconel substrate holder and heated by a radiative heater. The substrate temperature was varied from room temperature to 200 °C. The depositions were performed for 120 min, that resulted in film thicknesses in the 80 to 120 nm range.

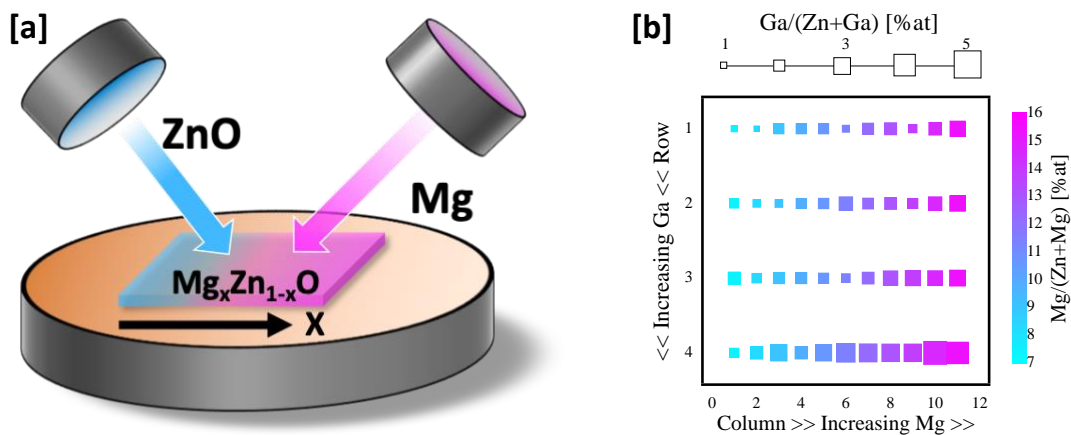


Figure 1. [a] Combinatorial sputter deposition of $\text{Mg}_x\text{Zn}_{1-x}\text{O}$ thin films. [b] 4×11 composition measurement grid for $\text{Ga}:\text{Mg}_x\text{Zn}_{1-x}\text{O}$ films on a $50\text{mm} \times 50\text{mm}$ glass substrate.

Each sample was characterized at 4×11 grid points with the following spatially resolved methods (Figure 1b). X-ray diffraction (XRD) patterns for the MZO thin films were obtained using a Bruker D8 Discover XRD instrument. Electrical resistivity/conductivity data was measured by a custom four-point probe system; the highest measurable sheet resistance by the equipment is $\sim 5 \times 10^7 \Omega/\square$. Optical absorption was measured with a custom UV/Vis/NIR Spectroscopy system equipped with an OceanOptics DH-2000-BAL deuterium-halogen light source and a StellerNet EPP2000-UVN-SR spectrometer. The chemical compositions of the films, atomic $\text{Ga}/(\text{Ga}+\text{Zn})$ ratio, were measured with a Fisherscope XUV-733 X-ray fluorescence (XRF) instrument. Mg, being a light element, was quantified using Rutherford backscattering spectroscopy (RBS) and energy dispersive x-ray spectrometry (EDX). EDX data was taken using an acceleration voltage of 5.0 keV. For Mg quantification purpose, 10×10 mm glassy carbon or silicon witness substrates were placed at the 2nd row of the 4×11 sample library grid. The use of such impurity free witness substrates reduced background noise in quantification of light elements in small amounts. Experimental combinatorial data collected in this study were managed, analyzed and displayed using our publicly available COMBIgor software package for Igor Pro [32], and will be made available through the High Throughput Experimental Materials Database (HTEM DB) [33].

Kelvin probe measurement system from KP technology was used to determine the work function for both the MZO (on doped Si substrates) and CuGa_3Se_5 (on Mo coated glass substrates) films. A gold reference (work function 5.1 eV) in air was used to quantify the absolute value of the surface potentials. X-ray photoelectron spectroscopy (XPS) was performed on the CuGa_3Se_5 films using monochromatic Al $K\alpha$ radiation and a pass energy of 29 eV. The spectrometer binding

energy scale was calibrated at high and low energy using clean gold and copper foils and known transition energies. Data analysis and peak fitting were performed using a combination of Igor and PHI MultiPak.

Cross-section scanning electron microscopy (SEM) image of the device was taken with a Hitachi S-4800 SEM instrument operated at 2kV. Cross-section transmission electron microscopy (TEM) specimens were prepared using the focused ion beam (FIB) lift out technique with the final Ga⁺ ion milling performed at 3 kV. Ga⁺ ion FIB damage was subsequently removed using low energy (< 1kV) Ar⁺ ion milling in a Fischione Nanomill with the sample cooled by liquid nitrogen. Scanning transmission electron microscopy (STEM) imaging and EDX mapping analysis were performed in a FEI Tecnai F20 UltraTwin field emitting gun STEM operated at 200 kV and equipped with an EDAX Octane T Optima Si drift detector (SDD) EDX system.

2.2 Device fabrication and characterization

Substrates for device fabrication were soda-lime glass. Mo back contact was deposited by Direct Current sputtering. Near stoichiometric CuGa₃Se₅ thin films with Cu/Ga = 0.36 composition were deposited by three-stage co-evaporation (Ga-Se in the 1st stage, Cu-Se in the 2nd stage, and Ga-Se in the 3rd stage) at 600 °C. For comparison, a baseline device was fabricated in a similar fashion to narrow bandgap (~1.1 eV) CIGS absorber devices, more details on the process steps can be found elsewhere [9] [34]. The solution for Cd²⁺ surface treatment contained 2mM CdSO₄ in NH₄OH and DI water, and no S precursor. Only device data containing undoped MZO is presented here, as they produced superior devices.

PEC characteristics of the devices were measured by performing chopped-light linear sweep voltammograms (LSV) in a three-electrode configuration with CuGa₃Se₅ photocathode, Pt counter electrode, and Ag/AgCl reference electrode with 3M NaCl filling solution.

Photoelectrodes were made by indium bonding an insulated Cu wire to an exposed part of the Glass/Mo substrate. A number of different electrolyte solutions was tested, including (1M Na₂SO₄ + pH7 buffer), (NaOH + H₂SO₄ + 0.5M Na₂CO₃, pH = 9.6), and (0.5M Na₂SO₄ + 0.25M KH₂PO₄ + 0.25M K₂HPO₄, pH = 6.7), yet the CuGa₃Se₅/MZO thin films were found to be unstable in all of these solutions with the photocurrent limited due to charge transport. As such, LSV analyses were performed in a solution containing 10 mM hexaammineruthenium (III) chloride, 0.5M KCl and pH7 buffer. During the measurements, the samples were illuminated with a 300 W Xenon arc lamp (Newport) through an AM 1.5G filter (Oriel), simulating one-sun equivalent illumination as adjusted using a calibrated 1.8 eV GaInP₂ PV reference cell. The electrode device area was defined by nonconductive epoxy (Loctite 9462), which isolated the wire and Mo substrate from the electrolyte. The device areas were measured by counting the number of pixels from digitally scanned images of the electrodes. Potentials are reported against the reversible hydrogen electrode by using the relationship $E(\text{RHE}) = E_{\text{Ag}/\text{AgCl}} + 0.059 \times \text{pH} + E_{0, \text{Ag}/\text{AgCl}}$, where $E_{0, \text{Ag}/\text{AgCl}} = 0.209\text{V}$. The standard reduction potential (E^0) for the hexaammineruthenium redox couple is 0.1 V vs RHE [35].

For PV device fabrication, Al:ZnO (120 nm) as transparent conductive oxide was deposited by RF magnetron sputtering, and Ni(50 nm)/Al(3 μm) front grids by e-beam evaporation [34]. Solar cell performance was characterized based on photocurrent density-voltage (JV) and quantum efficiency (QE) performances. JV data for the combinatorial device library was collected with a custom made automated XY probe station under AM1.5 light from an Oriel 91194-1000 solar simulator with the samples maintained at 20 °C. External QE for select devices were measured with a Newport Oriel IQE-200.

3. Results and Discussions:

3.1 $\text{Mg}_x\text{Zn}_{1-x}\text{O}$ thin film characterization:

For CuGa_3Se_5 device integration, combinatorial RF sputtered $\text{Mg}_x\text{Zn}_{1-x}\text{O}$ was deposited with x values in the 0 to 0.15 range, and $\text{Ga}/(\text{Ga}+\text{Zn})$ atomic ratio from 0% to 15%. Figure 1b shows the composition profile of one such $\text{Ga}:\text{Mg}_x\text{Zn}_{1-x}\text{O}$ library, and RBS data for a selected sample is presented in Figure S1. XRD patterns of the MZO films were all (0002) oriented wurtzite ZnO ; no peaks related to MgO or Ga_2O_3 secondary phases were observed for the investigated span of Mg and Ga compositions (Figure 2). With increasing Mg composition, the ZnO (0002) peak broadened, intensity reduced and shifted towards lower angles. This shift was more significant at higher $\text{Ga}/(\text{Ga}+\text{Zn})$ samples. Mg atomic size is much lower than Zn or Ga. Mg incorporation at large degree could induce strain in the ZnO crystal, indicated by the peak broadening at high Mg samples.

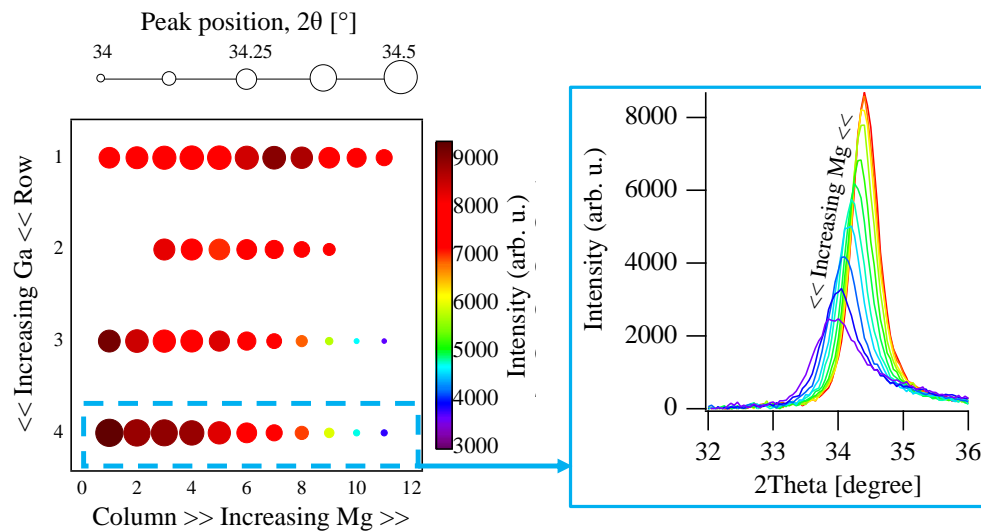


Figure 2. ZnO (0002) peak position and intensity for a $\text{Ga}:\text{Mg}_x\text{Zn}_{1-x}\text{O}$ sample library deposited at 200°C .

The film conductivity for the undoped MZO films deposited at 100°C or below were too low to be measured. The conductivity for the doped MZO films were dependent on Ga and Mg compositions (Figure 3a). Conductivity decreased with increasing Mg composition, possibly due to wider bandgap and increased carrier scattering. Introduction of Ga as dopant increased conductivity, and then decreased it at higher Ga concentrations when Ga/(Ga+Zn) atomic ratio exceeded 5%. This was likely due to the reduced crystallinity of those samples, as evident from the XRD data. The highest conductivity was 20 S/cm and was observed at Ga/(Ga+Zn) value of 4%. Mg incorporation also resulted in the expected bandgap widening. Increasing Mg composition increased the optical bandgap of MZO, calculated from the Tauc plot of the absorption data from UV-Vis spectroscopy (Figure 3b). For the highest experimented Mg composition of 13%, optical band gap values up to 3.57 eV was estimated.

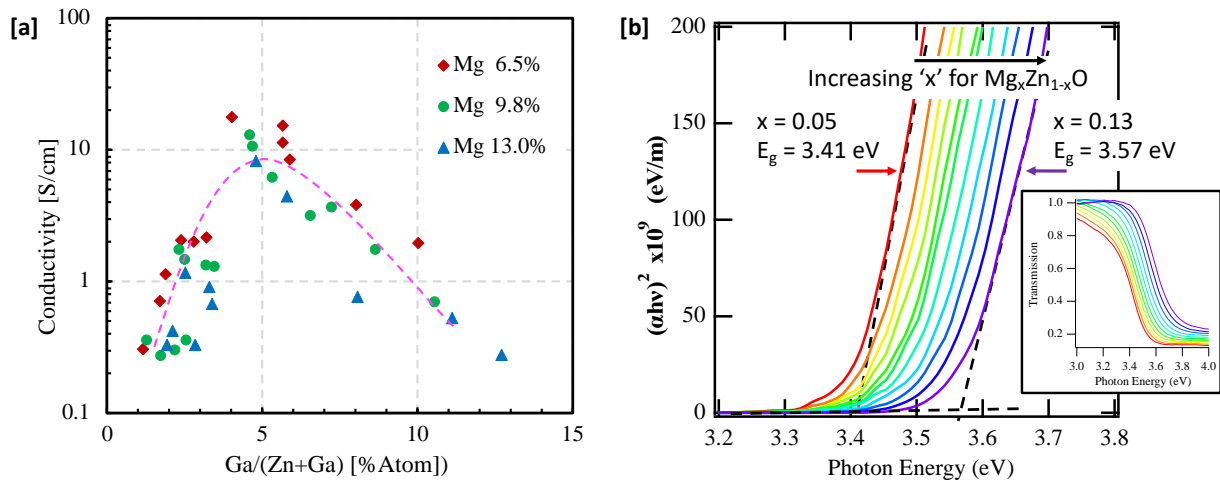


Figure 3. [a] Conductivity vs. Ga/(Ga+Zn) atomic ratio for Mg_xZn_{1-x}O:Ga thin films deposited at 200°C. [b] Tauc plot from the transmittance data showing the shift in the estimated optical bandgap for undoped MZO films with increasing Mg composition.

3.2 Photoelectrochemical Characteristics:

The PEC characteristics of the CuGa₃Se₅ photocathodes were investigated with chopped light linear sweep voltammetry (LSV) with a 3-electrode system under simulated AM1.5G illumination. The LSV data is shown in supplement Figure S2, for analysis performed in hexaammineruthenium (III) chloride redox mediator and KCl supporting electrolyte with pH7 buffer. It should be noted that LSV measurement performed with a sacrificial redox agent is not water splitting, however it gives an estimate of the quality of the device characteristics. There was sign of degradation during consecutive testing, however that could be due to scanning near high anodic potentials. The dark current was nearly zero. The photocurrent saturated at more cathodic potentials. The initial current transient could be due to charge transport limitation in the electrolyte and/or at the electrode surface. The photocurrent onset potentials extrapolated from the LSV curves are shown in Table 1.

Table 1. Photocurrent onset potentials from the LSV data

Electrode	V _{onset} (V vs. RHE)
CuGa ₃ Se ₅ (As Deposited)	0.57 ± 0.02
CuGa ₃ Se ₅ /(Cd ²⁺)	0.64 ± 0.02
CuGa ₃ Se ₅ /CdS/i-ZnO	1.18 ± 0.04
CuGa ₃ Se ₅ /(Cd ²⁺)/i-MZO	1.08 ± 0.03

The untreated Mo/CuGa₃Se₅ electrode had a photocurrent onset potential (V_{onset}) of ~0.57 V vs. RHE. The Fermi level of the p-type CuGa₃Se₅ semiconductor would be located much lower than the solution potential (reduction potential of the redox). This would create a charge depletion layer in the semiconductor due to transfer of valence band hole to the solution. In equilibrium, this charge separation would form a built-in electric field, causing a downward band bending. The

potential V_{onset} is indicative of this built-in potential. An increase of V_{onset} up to 0.64 V vs. RHE, for Cd^{2+} solution treated CuGa_3Se_5 electrode indicated an increase of this band bending.

For $\text{CuGa}_3\text{Se}_5/\text{n-CdS}/\text{i-ZnO}$ device, V_{onset} close to 1.2 V vs. RHE was observed. This was indicative of the good interface passivation and/or extended depletion region due to increased band bending at the pn-junction formed between n-CdS and p- CuGa_3Se_5 . The optimized $\text{CuGa}_3\text{Se}_5/(\text{Cd}^{2+})/\text{MZO}$ devices also exhibited V_{onset} potential near 1.0 V vs. RHE. However, this value for devices with Cd^{2+} treated absorber surfaces was lower compared to baseline CdS devices. This difference in the onset potential could not be due to substitution of MZO for i-ZnO alone, since $\text{CuGa}_3\text{Se}_5/\text{MZO}$ solid-state stacks resulted in no photo-response. Even with the absence of an evident active n-type layer, the $\text{CuGa}_3\text{Se}_5/(\text{Cd}^{2+})/\text{MZO}$ devices still exhibited V_{onset} potential above 1V vs. RHE. This encouraging result indicated that Cd^{2+} treatment itself introduced a surface passivation and/or a band bending at the absorber interface. However, for $(\text{Cd}^{2+})\text{-MZO}$ (undoped) modified electrode the band bending must be lower compared to the CdS modified electrode, evident from the onset potential values. A schematic of the equilibrium band diagram for a $\text{CuGa}_3\text{Se}_5/\text{MZO}$ photoelectrode is shown in the supplement Figure S2 inset.

3.3 Surface and Interface:

To better understand the PEC characteristics of the electrodes, the absorber surface and interface modification due to the Cd^{2+} solution treatment was further investigated. Surface sensitive XPS/UPS of the as-deposited and treated CuGa_3Se_5 revealed how the wet treatment affected the absorber surface (Figure 4). The XPS survey spectrum of the as-deposited CuGa_3Se_5 is shown in the supplement Figure S3. The surface doping of as grown CuGa_3Se_5 appeared stable over a period of months, and was only slightly p-type (the XPS measurement on the as grown

sample was repeated after 3 months, data not shown). The valence band position ($E_F - E_{VBM}$) value measured with monochromatic Al K_α and He I excitation was 0.55 eV and 0.72 eV respectively (supplement Figure S4). UPS results with He I light (21.2 eV) had a probe depth of less than 1 nm in the sample surface, while VBM measurements with Al K_α (1487 eV) measured up to 10 nm into the bulk of the film due to higher photoelectron kinetic energy. This indicated the presence of a downward band bending at the as-grown surface.

The elemental compositions of the $CuGa_3Se_5$ surface with different treatments is shown in Table 2. There were a number of changes that happened with both NH_4OH and Cd^{2+} (65°C 15 min) treatments (Figure 4). A high degree of surface oxidation is observed for as deposited absorber, along with Na diffused from the soda lime glass substrate. With both NH_4OH and Cd^{2+} treatments, surface Na was removed and the O quantity was reduced. The gallium $2p_{3/2}$ peak narrowed significantly with Cd^{2+} treatment, probably due to the removal of gallium oxides. It is also interesting to note that the cadmium solution treatment (and likely the subsequent air exposure), caused the appearance of oxidized selenium, Se^{4+} . For CdTe devices a very thin layer of oxidized tellurium was found to be critical for well-passivated interfaces [36]. Such Se oxidation could also be beneficial for surface passivation of the $CuGa_3Se_5$ absorbers studied here.

No Cd could be detected on the Cd^{2+} treated $CuGa_3Se_5$ films using XRF and SEM/EDX analysis techniques, which are more sensitive to the bulk than XPS. Such comparison of XPS and EDX (probes deeper, up to 100 nm) and XRF (probes up to 1000 of nm) compositions for as-grown films indicated a Cu deficiency on the surface which is likely due to the sites being replaced by Na atoms. Cd^{2+} treatment introduced Cd on the absorber surface (supplement Figure S3). Exposure of the surface to aqueous cadmium sulfate likely caused an ion exchange process between cadmium and copper. Removal of Na atoms by NH_4OH could allow Cd atoms to occupy

these sites and change surface doping. The ($E_F - E_{VBM}$) values from XPS and work function values from Kelvin probe measurement for differently treated films also suggested a change in surface doping.

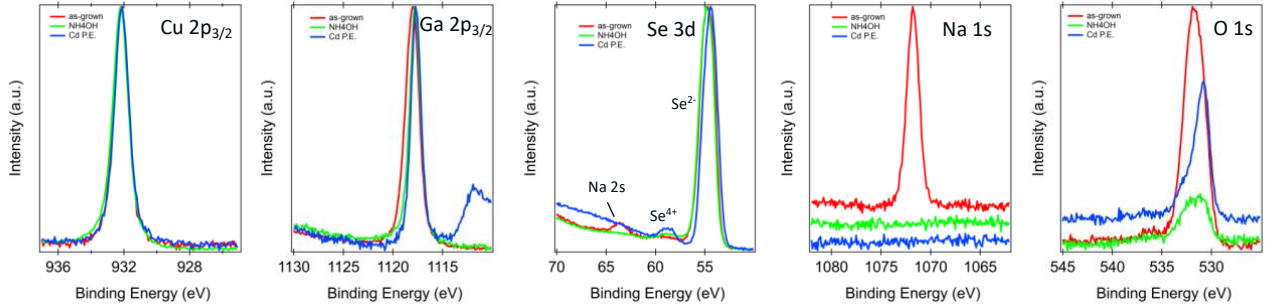


Figure 4. Elemental core levels of the CuGa_3Se_5 surface with different surface treatments, measured by XPS.

Table 2. XPS and EDX composition of untreated and treated CuGa_3Se_5 absorber.

CuGa_3Se_5	Technique	O (%)	Na (%)	Cu (%)	Ga (%)	Se (%)	Cd (%)
As Deposited	XPS	41.8	7.9	3.4	24.5	22.5	-
		(normalized)		6.7	48.6	44.7	-
	XRF	-	-	11.2	32.5	55.6	-
	EDS	-	-	14.2	45.1	40.7	-
NH_4OH treatment	XPS	10.9	-	18.4	25.1	45.7	-
		(normalized)		20.6	28.1	51.3	-
Cd^{2+} treatment	XPS	21.2	-	4.8	19.8	35.8	18.4
		(normalized)		8.0	32.7	59.3	

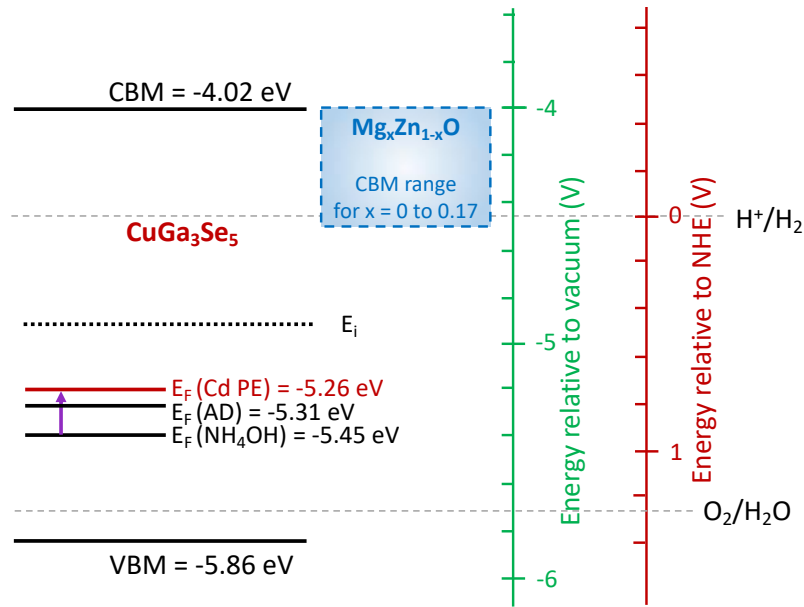


Figure 5. Energy band positions for CuGa_3Se_5 absorber with different surface treatments, in comparison with the CBM position in $\text{Mg}_x\text{Zn}_{1-x}\text{O}$.

Figure 5 shows the band diagram for CuGa_3Se_5 with Fermi energy level (E_F) positions for different treatments. The E_F values with respect to valence band maximum (E_{VBM}) are derived from XPS measurements. The change in E_F with different surface treatments were further validated with relative work function values from Kelvin probe measurements. CBM energy level was calculated using the bandgap value of 1.84 eV for CuGa_3Se_5 . For as deposited bulk thin films, $E_F - E_{\text{VBM}} = 0.28$ eV was calculated using the carrier concentration of $\sim 2 \times 10^{14} \text{ cm}^{-3}$ from Hall effect measurement and the carrier effective masses were obtained from literature [37]. The attainable CBM range for MZO is from our previous combinatorial study [27].

An $E_F - E_{\text{VBM}}$ of 0.55 eV for the as deposited absorber surface suggested a downward band bending with reduced p-type conductivity. A NH_4OH treatment lowered the value to 0.41 eV due to the removal of surface states. $E_F - E_{\text{VBM}}$ increased to 0.6 eV with Cd^{2+} treatment, likely due to Cd replacing Cu, creating compensating defect(s) on the absorber surface. This implied a shift in

surface conductivity type towards becoming intrinsic. Cadmium did not appear to dope the surface fully n-type, unlike what was reported for CIGSe or CISE [38] [39]. CIGSe and CISE normally are p-type at the surface and after cation exchange with cadmium solution, become n-type. However, Cd^{2+} treatment for CuGa_3Se_5 only moved the Fermi level upward, closer to being intrinsic.

3.4 Photovoltaic characterization:

To understand the influence of the contact CB position on the absorber performance in PEC environment, $\text{Mg}_x\text{Zn}_{1-x}\text{O}$ with varying composition was integrated with CuGa_3Se_5 absorbers into solid state test structures with top TCO and metal contacts. For the baseline PV device ($\text{CuGa}_3\text{Se}_5/\text{CdS}/\text{i-ZnO}$ material stack), the open circuit voltage ($V_{\text{OC}} = 730$ mV, short-circuit current ($J_{\text{SC}} = 5.7$ mA/cm², fill factor (FF) = 61%, and efficiency 2.6% were achieved. Initial devices with CdS contact layer, and MZO layer replacing i-ZnO layer showed promising results: $V_{\text{OC}} = 755$ mV, $J_{\text{SC}} = 7.6$ mA/cm², FF = 38.4%, and efficiency 2.1% (Supplementary Figure S5). A clear CdS layer was observed in SEM (Figure 6a), STEM/HAADF (Figure 6c) and STEM/EDX (Figure 6e) images.

$\text{Mg}_x\text{Zn}_{1-x}\text{O}$ was then studied as a replacement for the CdS/i-ZnO contact stack. PV devices without any surface treatment of the as-deposited CuGa_3Se_5 didn't exhibit any quantifiable current generation. Solution treatments of CuGa_3Se_5 indicated a pathway to replace CdS with MZO, with MZO grown directly on NH_4OH -treated and Cd^{2+} solution treated CuGa_3Se_5 surfaces. The NH_4OH treatment of the absorber prior to MZO deposition resulted in some photovoltaic activity, although the device performance values were quite low. Cd^{2+} solution treated CuGa_3Se_5 surfaces led to improved PV performance, and some incorporation of Cd into CuGa_3Se_5 surfaces.

The material stack for the PV devices with Cd-treated CuGa_3Se_5 absorbers and MZO contacts are shown in Figure 6b. The effect of the Cd^{2+} solution treatment could not be resolved from the SEM (Figure 6b) or STEM/HAADF (Figure 6d) images, indicating that very small amount of Cd was substituted at the surface (as indicated by XPS). However, STEM/EDX elemental map of the device revealed Cd present at the CuGa_3Se_5 /MZO interface (Figure 6f). Elemental line profiles from STEM/EDX showing the change in elemental composition across the cross section for these devices is shown in supplementary Figure S6. A small amount of Sulphur (S) is also present at this interface, which is likely due to CdSO_4 that was the source of Cd^{2+} .

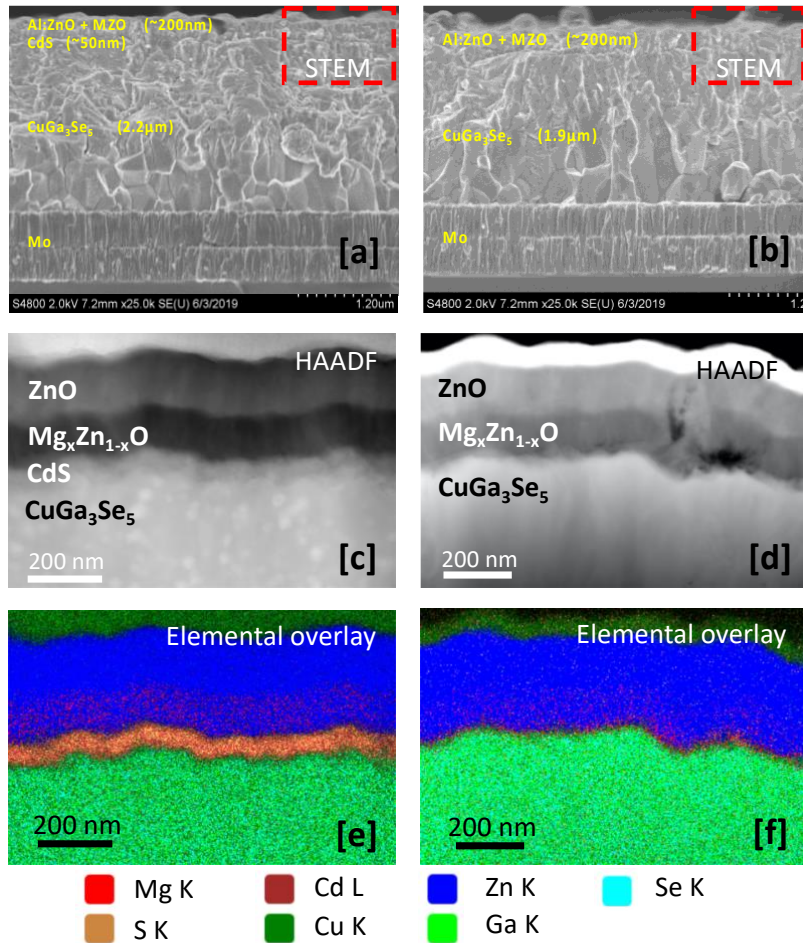


Figure 6. (a, b) SEM images with color overlay for the PV devices. (c, d) STEM HAADF images and (e, f) STEM EDX elemental maps at the $\text{CuGa}_3\text{Se}_5/\text{MZO}$ interfaces. $\text{CuGa}_3\text{Se}_5/\text{MZO}$ PV device with CdS (a, c, e), and Cd^{2+} solution treatment (b, d, f).

The device performances were dependent on the temperature and the duration of the Cd^{2+} treatment (Figure 7). Lower treatment temperature (65°C 15 min) improved the V_{OC} up to 925 mV, while higher temperature (85°C 7 min) treatment resulted in higher J_{SC} up to 8.3 mA/cm^2 (Figure 7c and Table 3). The highest open circuit voltage of 925 mV was observed for Mg composition of 10% in MZO (Figure 7a). Comparing QE of different device configurations (Figure 7b) showed that replacing CdS with $\text{Mg}_x\text{Zn}_{1-x}\text{O}$ improved the carrier collection in the short wavelengths due to the higher bandgap of MZO. As shown previously, the conductivity of $\text{Mg}_x\text{Zn}_{1-x}\text{O}$ could be improved by doping with Ga, which required higher substrate temperature. However, device performance was significantly reduced with V_{OC} in the range of 400 to 500 mV and many devices with doped MZO were shunted (data not shown), possibly due to the higher temperature exposure.

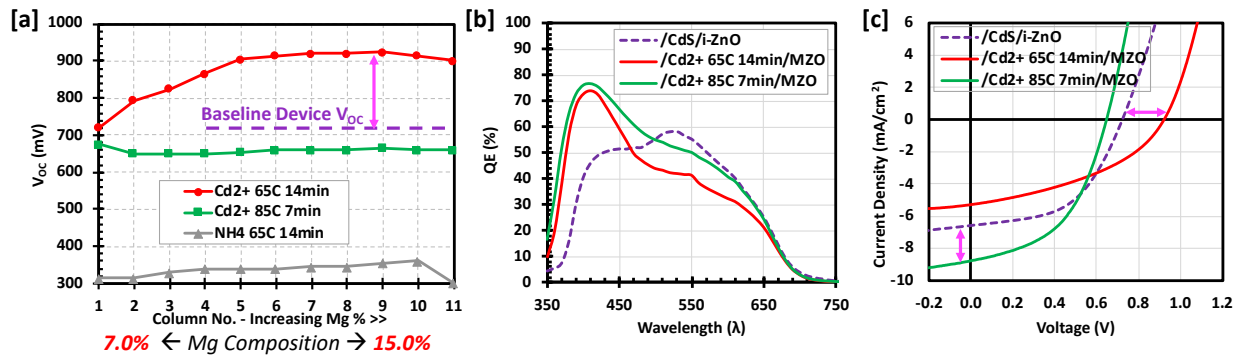


Figure 7. PV performance for CdS-free $\text{CuGa}_3\text{Se}_5/\text{Mg}_x\text{Zn}_{1-x}\text{O}$ devices with different surface treatments, including [a] open circuit voltage, [b] external quantum efficiency, and [c] current voltage characteristics.

The photovoltaic device performance for various configurations are summarized in Table 3. Although significant open-circuit voltage improvement was observed in MZO based devices, the fill factor and photocurrent output were reduced. The $\text{CuGa}_3\text{Se}_5/(\text{Cd}^{2+})/\text{MZO}$ photovoltaic devices had superior open-circuit voltage of 925 mV compared to 730 – 755 mV for CdS based devices. Looking at the complete device structure, $\text{CuGa}_3\text{Se}_5/(\text{Cd}^{2+})/\text{Mg}_x\text{Zn}_{1-x}\text{O}/\text{Al}:\text{ZnO}/\text{metal}$ grid, the n-type counterpart for the p-type CuGa_3Se_5 absorber in this case is likely $\text{Mg}_x\text{Zn}_{1-x}\text{O}/\text{Al}:\text{ZnO}$ bilayer. Change of absorber surface conductivity type to either intrinsic or slightly n-type could create a better p-i-n junction that improved the device V_{OC} , where bulk of the CuGa_3Se_5 absorber is the p-type layer, the $\text{Mg}_x\text{Zn}_{1-x}\text{O}/\text{Al}:\text{ZnO}$ is the n-type bilayer stack, and the Cd^{2+} -treated CuGa_3Se_5 surface is the intrinsic (i) layer.

Table 3. Photovoltaic device performance for different configurations

Device Configuration	V_{OC} (mV)	J_{SC}	FF (%)	Efficiency (%)
CGS/CdS/i-ZnO	730	5.7	61.4	2.6
CGS/CdS/MZO	755	7.6	38.4	2.1
CGS/ Cd^{2+} 65°C 14min/MZO	925	4.8	41.9	1.9
CGS/ Cd^{2+} 85°C 7min/MZO	650	8.3	47.6	2.6

$\text{Mg}_x\text{Zn}_{1-x}\text{O}$ contacted CuGa_3Se_5 absorber PV device data fulfilled two important requirements for top cell tandem device application: high V_{OC} and improved QE in the blue region of the spectrum. Although direct water splitting tests were not performed yet due to the instability of MZO in acidic solutions, LSV testing in sacrificial redox couple showed promising outcomes. A thin protective layer deposited on top of MZO could improve stability and facilitate water splitting experiments. More experiments are in progress to integrate such protective coatings on MZO without degrading underlying absorber/contact interface, and will be reported in the future.

4. Conclusion:

Mg_xZn_{1-x}O contact integration with CuGa₃Se₅ absorber has been demonstrated. MZO deposition and absorber surface treatment parameters are determined for improved photovoltaic device performance, which allowed the elimination of the CdS contact layer. Characterization of the CuGa₃Se₅ films with Cd²⁺ solution surface treatment indicated that the beneficial effect of the treatment is due to removal of surface oxidation and change in surface doping by Cd substitution. The photoelectrochemical characteristics of the devices were promising for future water splitting applications: from linear sweep voltammetry in 10 mM hexaammineruthenium (III) chloride, a photocurrent onset potential near 1V vs RHE was observed. For solid state PV devices, replacing CdS/i-ZnO with MZO improved the carrier collection in the short wavelengths and resulted in open circuit voltage of 925 mV, which is promising for top-cell tandem PV device applications. The results of this research will facilitate the understanding of CuGa₃Se₅/Mg_xZn_{1-x}O interface, and the use of CuGa₃Se₅ absorbers for both PEC and PV device applications.

Acknowledgements

This work was authored in part by the National Renewable Energy Laboratory (NREL), operated by Alliance for Sustainable Energy LLC, for the U.S. Department of Energy (DOE) under contract no. DE-AC36-08GO28308. Funding provided by the Office of Energy Efficiency and Renewable Energy (EERE), under Fuel Cell Technologies Office (FCTO), as a part of HydroGEN Energy Materials Network (EMN) consortium project administrated by the University of Hawaii under contract no. DE-EE0006670. The authors would like to acknowledge John Perkins and

Bobby To of NREL for the RBS analysis and SEM images respectively. The views expressed in the article do not necessarily represent the views of the DOE or the U.S. Government.

References

- [1] K. Christopher and R. Dimitrios, “A review on exergy comparison of hydrogen production methods from renewable energy sources,” *Energy and Environmental Science*, vol. 5, no. 5, pp. 6640–6651, May-2012, doi: 10.1039/c2ee01098d.
- [2] A. Fujishima and K. Honda, “Electrochemical photolysis of water at a semiconductor electrode,” *Nature*, vol. 238, no. 5358, pp. 37–38, 1972, doi: 10.1038/238037a0.
- [3] E. L. Miller, B. Marsen, D. Paluselli, and R. Rocheleau, “Optimization of hybrid photoelectrodes for solar water-splitting,” *Electrochem. Solid-State Lett.*, vol. 8, no. 5, pp. 247–249, 2005, doi: 10.1149/1.1887196.
- [4] W. H. Cheng *et al.*, “Monolithic Photoelectrochemical Device for Direct Water Splitting with 19% Efficiency,” *ACS Energy Lett.*, vol. 3, no. 8, pp. 1795–1800, Aug. 2018, doi: 10.1021/acsenerylett.8b00920.
- [5] N. Gaillard, D. Prasher, J. Kaneshiro, S. Mallory, and M. Chong, “Development of Chalcogenide Thin Film Materials for Photoelectrochemical Hydrogen Production,” *MRS Proc.*, vol. 1558, pp. mrss13-1558-z02-07, Oct. 2013, doi: 10.1557/opl.2013.1084.
- [6] M. Moriya, T. Minegishi, H. Kumagai, M. Katayama, J. Kubota, and K. Domen, “Stable hydrogen evolution from cds-modified CuGaSe₂ photoelectrode under visible-light irradiation,” *J. Am. Chem. Soc.*, vol. 135, no. 10, pp. 3733–3735, 2013, doi: 10.1021/ja312653y.
- [7] A. D. Deangelis, K. Horsley, and N. Gaillard, “Wide Band Gap CuGa(S,Se)₂ Thin Films on Transparent Conductive Fluorinated Tin Oxide Substrates as Photocathode Candidates for Tandem Water Splitting Devices,” *J. Phys. Chem. C*, vol. 122, no. 26, pp. 14304–14312,

- 2018, doi: 10.1021/acs.jpcc.8b02915.
- [8] N. Gaillard *et al.*, “Wide-Bandgap Cu(In,Ga)S₂ Photocathodes Integrated on Transparent Conductive F:SnO₂ Substrates for Chalcopyrite-Based Water Splitting Tandem Devices,” *ACS Appl. Energy Mater.*, p. acsaem.9b00690, 2019, doi: 10.1021/acsaem.9b00690.
- [9] C. P. Muzzillo *et al.*, “Low-Cost, Efficient, and Durable H₂ Production by Photoelectrochemical Water Splitting with CuGa₃Se₅ Photocathodes,” *ACS Appl. Mater. Interfaces*, vol. 10, no. 23, pp. 19573–19579, 2018, doi: 10.1021/acsami.8b01447.
- [10] S. B. Zhang, S. H. Wei, and A. Zunger, “Stabilization of ternary compounds via ordered arrays of defect pairs,” *Phys. Rev. Lett.*, vol. 78, no. 21, pp. 4059–4062, 1997, doi: 10.1103/PhysRevLett.78.4059.
- [11] J. Kim, T. Minegishi, J. Kobota, and K. Domen, “Investigation of Cu-deficient copper gallium selenide thin film as a photocathode for photoelectrochemical water splitting,” *Jpn. J. Appl. Phys.*, vol. 51, no. 1, pp. 1–6, 2012, doi: 10.1143/JJAP.51.015802.
- [12] L. C. Seitz, Z. Chen, A. J. Forman, B. A. Pinaud, J. D. Benck, and T. F. Jaramillo, “Modeling practical performance limits of photoelectrochemical water splitting based on the current state of materials research,” *ChemSusChem*, vol. 7, no. 5, pp. 1372–1385, 2014, doi: 10.1002/cssc.201301030.
- [13] J. Kim, T. Minegishi, J. Kobota, and K. Domen, “Enhanced photoelectrochemical properties of CuGa₃Se₅ thin films for water splitting by the hydrogen mediated co-evaporation method,” *Energy Environ. Sci.*, vol. 5, no. 4, pp. 6368–6374, 2012, doi: 10.1039/c1ee02280f.
- [14] H. Kumagai, T. Minegishi, Y. Moriya, J. Kubota, and K. Domen, “Photoelectrochemical

- hydrogen evolution from water using copper gallium selenide electrodes prepared by a particle transfer method,” *J. Phys. Chem. C*, vol. 118, no. 30, pp. 16386–16392, Jul. 2014, doi: 10.1021/jp409921f.
- [15] S. Siebentritt and U. Rau, Eds., *Wide-Gap Chalcopyrites*. Springer, 2006.
- [16] M. Ruckh, D. Schmid, and H. W. Schock, “Photoemission studies of the ZnO/CdS interface,” *J. Appl. Phys.*, vol. 76, no. 10, pp. 5945–5948, 1994, doi: 10.1063/1.358417.
- [17] L. Weinhardt, C. Heske, E. Umbach, T. P. Niesen, S. Visbeck, and F. Karg, “Band alignment at the i-ZnO/CdS interface in Cu(In,Ga)(S,Se)₂ thin-film solar cells,” *Appl. Phys. Lett.*, vol. 84, no. 16, pp. 3175–3177, Apr. 2004, doi: 10.1063/1.1704877.
- [18] S. B. Zhang, S. H. Wei, and A. Zunger, “A phenomenological model for systematization and prediction of doping limits in II-VI and I-III-VI₂ compounds,” *J. Appl. Phys.*, vol. 83, no. 6, pp. 3192–3196, 1998, doi: 10.1063/1.367120.
- [19] M. Gloeckler and J. R. Sites, “Efficiency limitations for wide-band-gap chalcopyrite solar cells,” *Thin Solid Films*, vol. 480–481, pp. 241–245, 2005, doi: 10.1016/j.tsf.2004.11.018.
- [20] T. Song, A. Kanevce, and J. R. Sites, “Emitter/absorber interface of CdTe solar cells,” *J. Appl. Phys.*, vol. 119, no. 23, p. 233104, Jun. 2016, doi: 10.1063/1.4953820.
- [21] T. Minemoto *et al.*, “Theoretical analysis of the effect of conduction band offset of window/CIS layers on performance of CIS solar cells using device simulation,” *Sol. Energy Mater. Sol. Cells*, vol. 67, no. 1–4, pp. 83–88, Mar. 2001, doi: 10.1016/S0927-0248(00)00266-X.
- [22] T. Minemoto, T. Negami, S. Nishiwaki, H. Takakura, and Y. Hamakawa, “Preparation of Zn_{1-x}Mg_xO films by radio frequency magnetron sputtering,” *Thin Solid Films*, vol. 372,

- no. 1, pp. 173–176, Sep. 2000, doi: 10.1016/S0040-6090(00)01009-9.
- [23] A. Ohtomo *et al.*, “MgxZn1-xO as a II-VI widegap semiconductor alloy,” *Appl. Phys. Lett.*, vol. 72, no. 19, pp. 2466–2468, May 1998, doi: 10.1063/1.121384.
- [24] I. Takeuchi *et al.*, “Monolithic multichannel ultraviolet detector arrays and continuous phase evolution in MgxZn1-xO composition spreads,” *J. Appl. Phys.*, vol. 94, no. 11, pp. 7336–7340, Dec. 2003, doi: 10.1063/1.1623923.
- [25] L. A. Bendersky, I. Takeuchi, K. S. Chang, W. Yang, S. Hullavarad, and R. D. Vispute, “Microstructural study of epitaxial Zn1-xMg xO composition spreads,” *J. Appl. Phys.*, vol. 98, no. 8, p. 083526, Oct. 2005, doi: 10.1063/1.2061887.
- [26] S. Lautenschlaeger, J. Sann, P. J. Klar, M. Piechotka, and B. K. Meyer, “Combinatorial growth of MgxZn1-xO epilayers by chemical vapor deposition,” *Phys. Status Solidi Basic Res.*, vol. 246, no. 2, pp. 383–386, Feb. 2009, doi: 10.1002/pssb.200844347.
- [27] P. P. Rajbhandari, A. Bikowski, J. D. Perkins, T. P. Dhakal, and A. Zakutayev, “Combinatorial sputtering of Ga-doped (Zn,Mg)O for contact applications in solar cells,” *Sol. Energy Mater. Sol. Cells*, vol. 159, pp. 219–226, 2017, doi: 10.1016/j.solmat.2016.09.003.
- [28] T. Ablekim, E. Colegrove, and W. K. Metzger, “Interface Engineering for 25% CdTe Solar Cells,” *ACS Appl. Energy Mater.*, vol. 1, no. 10, pp. 5135–5139, 2018, doi: 10.1021/acsaem.8b01173.
- [29] J. Chantana, T. Kato, H. Sugimoto, and T. Minemoto, “20% Efficient Zn0.9Mg0.1O:Al/Zn0.8Mg0.2O/Cu(In,Ga)(S,Se)2 Solar Cell Prepared by All-Dry Process through a Combination of Heat-Light-Soaking and Light-Soaking Processes,” *ACS Appl.*

- Mater. Interfaces*, vol. 10, no. 13, pp. 11361–11368, 2018, doi: 10.1021/acsami.8b01247.
- [30] T. Minemoto, Y. Hashimoto, T. Satoh, T. Negami, H. Takakura, and Y. Hamakawa, “Cu(In,Ga)Se₂ solar cells with controlled conduction band offset of window/Cu(In,Ga)Se₂ layers,” *J. Appl. Phys.*, vol. 89, no. 12, pp. 8327–8330, 2001, doi: 10.1063/1.1366655.
- [31] A. Hultqvist, C. Platzer-Björkman, J. Pettersson, T. Törndahl, and M. Edoff, “CuGaSe₂ solar cells using atomic layer deposited Zn(O,S) and (Zn,Mg)O buffer layers,” *Thin Solid Films*, vol. 517, no. 7, pp. 2305–2308, Feb. 2009, doi: 10.1016/j.tsf.2008.10.109.
- [32] K. R. Talley *et al.*, “COMBIgor: Data-Analysis Package for Combinatorial Materials Science,” *ACS Comb. Sci.*, 2019, doi: 10.1021/acscombsci.9b00077.
- [33] A. Zakutayev *et al.*, “An open experimental database for exploring inorganic materials,” *Sci. Data*, vol. 5, no. 1, pp. 1–12, Apr. 2018, doi: 10.1038/sdata.2018.53.
- [34] M. A. Contreras *et al.*, “High efficiency Cu(In,Ga)Se₂-based solar cells: processing of novel absorber structures,” in *Conference Record of the IEEE Photovoltaic Specialists Conference*, 1994, vol. 1, pp. 68–75, doi: 10.1109/wcpec.1994.519811.
- [35] A. Bard and L. Faulkner, *Electrochemical methods, fundamentals and applications*, vol. 60, no. 1. 1983.
- [36] M. O. Reese *et al.*, “Intrinsic surface passivation of CdTe,” *J. Appl. Phys.*, vol. 118, no. 15, Oct. 2015, doi: 10.1063/1.4933186.
- [37] G. Marín, C. Rincón, S. M. Wasim, G. Sánchez Pérez, and I. Molina Molina, “Temperature dependence of the fundamental absorption edge in CuGa₃Se₅,” *J. Alloys Compd.*, vol. 283, no. 1–2, pp. 1–4, 1999, doi: 10.1016/S0925-8388(98)00878-0.
- [38] R. Hunger *et al.*, “SXPS investigation of the Cd partial electrolyte treatment of CuInSe₂

absorbers,” *Thin Solid Films*, vol. 480–481, pp. 218–223, 2005, doi: 10.1016/j.tsf.2004.11.115.

- [39] J. F. Han *et al.*, “TEM and XPS studies on CdS/CIGS interfaces,” *J. Phys. Chem. Solids*, vol. 75, no. 12, pp. 1279–1283, 2014, doi: 10.1016/j.jpcs.2014.06.002.

Supplementary Information

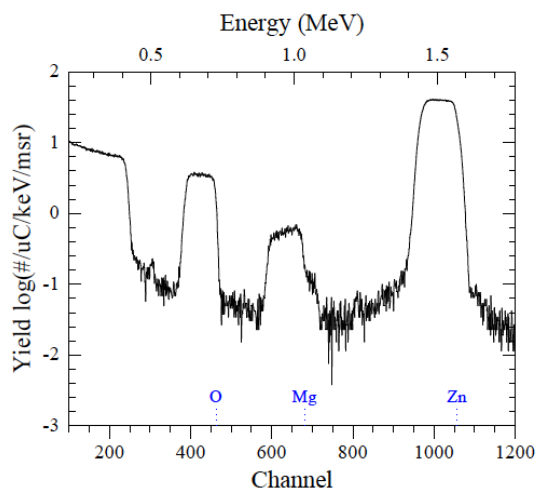


Figure S1. Rutherford Backscattering Spectroscopy (RBS) to quantify Mg composition of the MZO films.

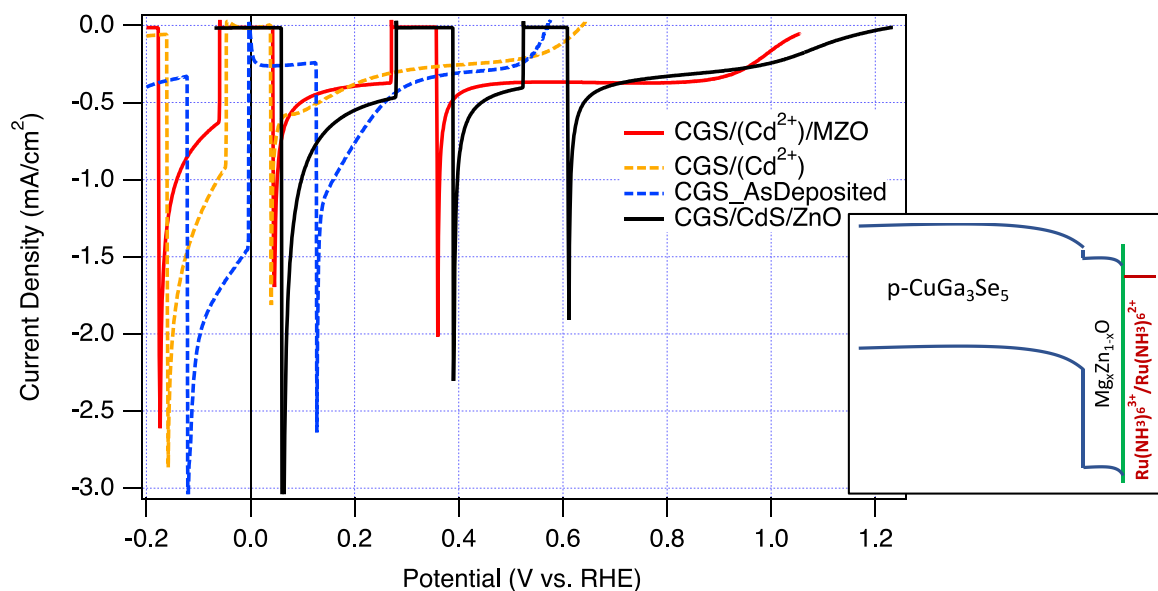


Figure S2. 3-electrode chopped light LSV measurement (in a solution containing 10 mM hexaammineruthenium (III) chloride, 0.5M KCl and pH7 buffer) data for CuGa₃Se₅ with different surface treatments and device configurations. (inset) A schematic of the equilibrium band diagram for CuGa₃Se₅/Mg_xZn_{1-x}O photoelectrode in sacrificial redox.

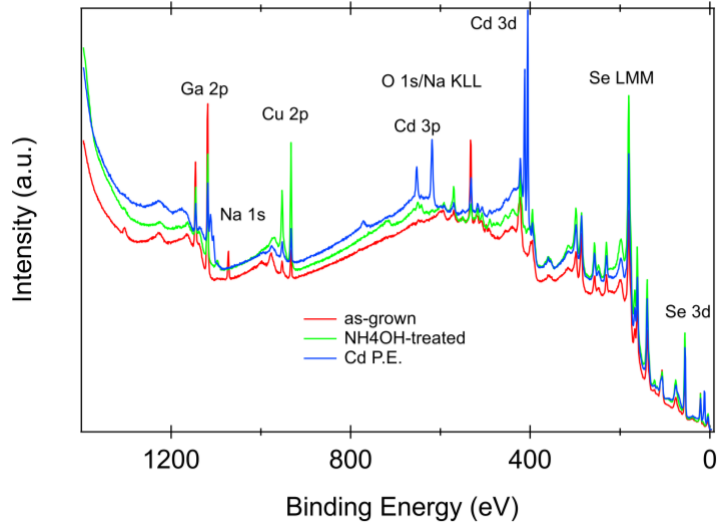


Figure S3. XPS survey spectrum of the as-deposited CuGa_3Se_5 film.

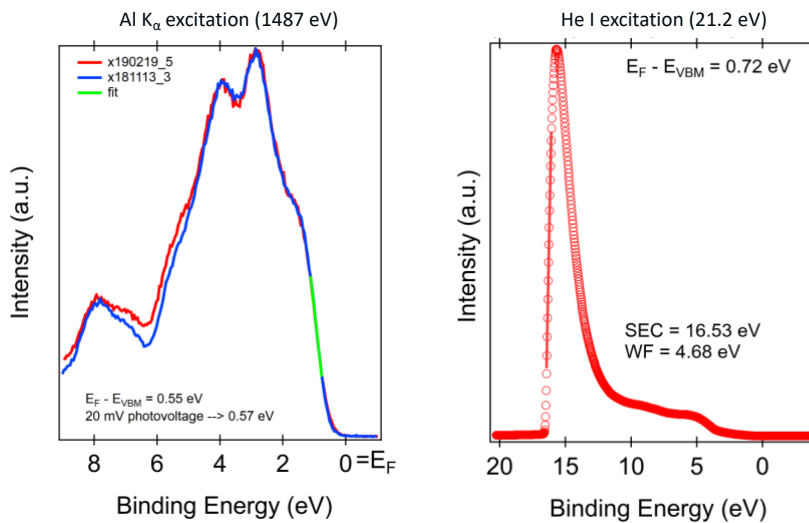


Figure S4. VBM position for as-deposited CuGa_3Se_5 film surface with $\text{Al K}\alpha$ and He I excitation.

$\text{CuGa}_3\text{Se}_5/\text{CdS}/\text{Mg}_x\text{Zn}_{1-x}\text{O}$ devices: A contact layer of $\text{Mg}_x\text{Zn}_{1-x}\text{O}$ with CdS improved the voltage and current output of the solar cells. Both V_{OC} and J_{SC} of the devices were function of the Mg composition in MZO (Figure S5). At low Mg composition, the performance was equivalent to the baseline device with *i*-ZnO contact layer. With increasing Mg concentration, both V_{OC} and

J_{SC} of the devices increased. Superior current output was reflected in the quantum efficiency (QE) data, where the overall QE of the devices were improved. At the longer wavelengths, carrier collection increased with increasing Mg concentration. Improved V_{OC} indicated favorable conduction band offset between CdS and MZO. Improved QE implied reduction in interface carrier recombination. However, the overall device photo-conversion efficiency was reduced due to lower fill factor. The best result for $CuGa_3Se_5/CdS/MZO$ devices: $V_{OC} = 755$ mV, $J_{SC} = 7.6$ mA/cm², FF = 38.4%, and efficiency 2.1%

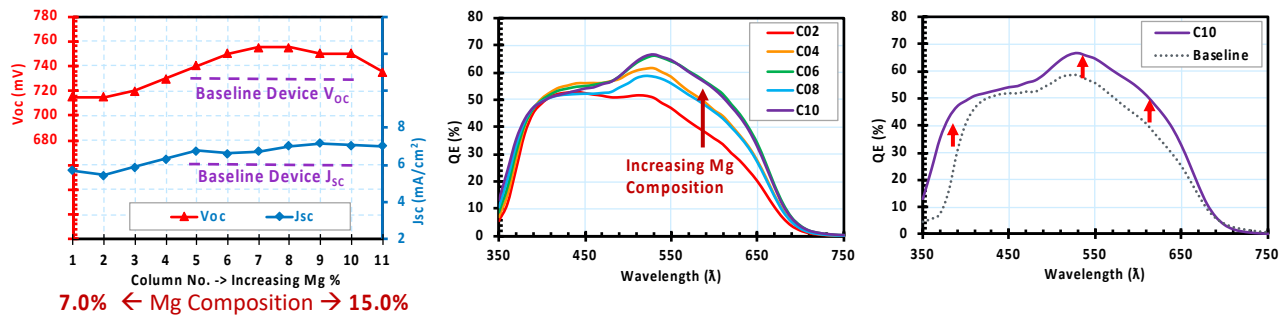


Figure S5. PV performance for $CuGa_3Se_5/CdS/Zn_{1-x}Mg_xO$ devices.

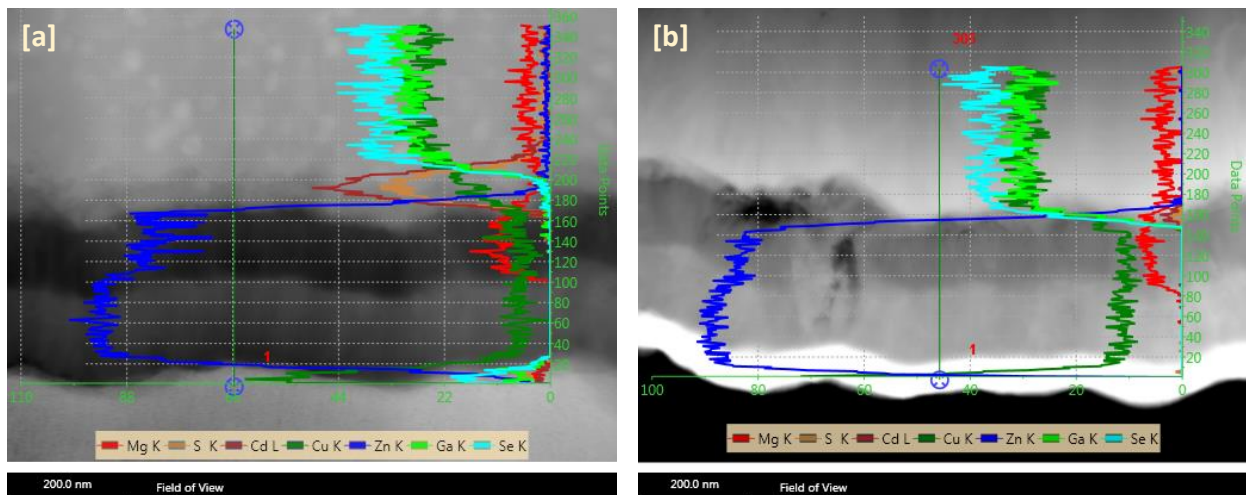


Figure S6. Elemental line profile from STEM/EDX overlaid on the STEM/HAADF image for $CuGa_3Se_5/MZO$ PV device with CdS [a], and Cd^{2+} solution treatment [b].